Dynamically hidden reaction paths in the reaction of CF3^+ + CO

Oda, Kohei
Graduate School of Chemical Sciences and Engineering, Hokkaido University

Tsutsumi, Takuro
Department of Chemistry, Faculty of Science, Hokkaido University

Keshavamurthy, Srihari
Department of Chemistry, Faculty of Science, Hokkaido University

Furuya, Kenji
Faculty of Arts and Science, Kyushu University

他

ACS PHYSICAL CHEMISTRY Au
AN OPEN ACCESS JOURNAL OF THE AMERICAN CHEMICAL SOCIETY

pubs.acs.org/physchemau Article

Dynamically Hidden Reaction Paths in the Reaction of CF_3^+ + CO

Kohei Oda, Takuro Tsutsumi, Srihari Keshavamurthy, Kenji Furuya,* P. B. Armentrout, and Tetsuya Taketsugu*

Cite This: https://doi.org/10.1021/acsphyschemau.2c00012 Read Online

ACCESS | Metrics & More | Article Recommendations | Supporting Information

ABSTRACT: Reaction paths on a potential energy surface are widely used in quantum chemical studies of chemical reactions. The recently developed global reaction route mapping (GRRM) strategy automatically constructs a reaction route map, which provides a complete picture of the reaction. Here, we thoroughly investigate the correspondence between the reaction route map and the actual chemical reaction dynamics for the CF_3^+ + CO reaction studied by guided ion beam tandem mass spectrometry (GIBMS). In our experiments, FCO^+, CF_2^+, and CF^+ product ions were observed, whereas if the collision partner is N_2, only CF_2^+ is observed. Interestingly, for reaction with CO, GRRM-predicted reaction paths leading to the CF^+ + F_2CO product channel are found at a barrier height of about 2.5 eV, whereas the experimentally obtained threshold for CF^+ formation was 7.48 ± 0.15 eV. In other words, the ion was not obviously observed in the GIBMS experiment, unless a much higher collision energy than the requisite energy threshold was provided. On-the-fly molecular dynamics simulations revealed a mechanism that hides these reaction paths, in which a non-statistical energy distribution at the first collisionally reached transition state prevents the reaction from proceeding along some reaction paths. Our results highlight the existence of dynamically hidden reaction paths that may be inaccessible in experiments at specific energies and hence the importance of reaction dynamics in controlling the destinations of chemical reactions.

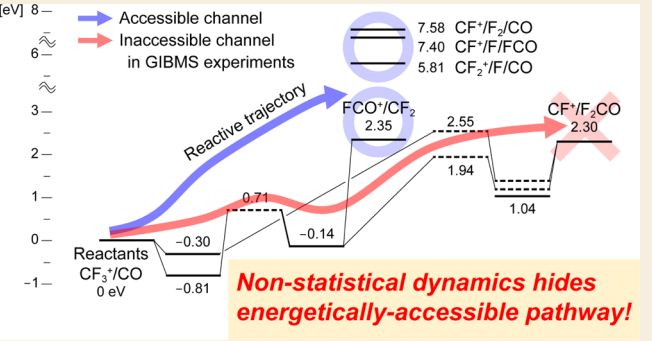

KEYWORDS: *non-statistical reaction dynamics, non-IRC reaction, guided ion beam tandem mass spectrometry, automated reaction path search, collision reaction, on-the-fly molecular dynamics, sudden vector projection*

1. INTRODUCTION

Under the Born-Oppenheimer approximation, a chemical reaction can be described using reaction paths on the potential energy surface (PES). The intrinsic reaction coordinate (IRC)[1,2] is a reaction path inherent to an elementary reaction that connects the structures of reactants, a transition state (TS), and products and provides an intuitive picture of the structural changes during the reaction. Recently, automated reaction path search methods such as the anharmonic downward distortion following (ADDF)[3,4] and the artificial force induced reaction[5] have emerged, making it possible to determine the reaction path without prior knowledge of the target reaction. These methods have led to a powerful concept called the global reaction route mapping (GRRM) strategy, which comprehensively finds numerous IRCs and dissociation paths on the PES. GRRM has elucidated various chemical reaction mechanisms.[6] In combination with TS theory, a method for efficient kinetic simulation based on the reaction route map obtained by GRRM has also been developed.[7] In these methods, assuming the validity of statistical approximations, chemical reactions are expected to proceed along multiple reaction paths that constitute the reaction route map.

It should be noted that the reaction path is determined solely on the basis of the shape of the PES. In other words, the reaction path does not take into account the dynamical effects of finite atomic momenta. Several early studies analyzed the dynamical effects on the basis of the reaction path curvature.[8,9] Nowadays, on-the-fly molecular dynamics (MD) is a powerful tool to study the dynamical effects of reaction processes by following the time evolution of nuclei with sequential electronic structure calculations. In 2002, Hase and co-workers proposed the concept of non-IRC dynamics from their observations that 90% of the trajectories of the OH^- + CH_3F reaction do not form the $CH_3OH\cdots F^-$ complex, the terminal point of the IRC, but lead directly to the dissociation products, CH_3OH + F^-.[10] It has been experimentally and theoretically confirmed that the reaction of F^- + CH_3OOH led to HF + CH_2O + OH^- and HF + CH_3OO^-,

Received: February 20, 2022
Revised: April 11, 2022
Accepted: April 13, 2022

which are different products compared to those from the terminus of the IRC, the $CH_2(OH)_2\cdots F^-$ complex.[11,12] This is probably a result of the large curvature of the IRC. Another important factor in the dynamical effects is bifurcation of the reaction path.[2] In organic and biological chemical reactions, there are sometimes unusual TSs, called ambimodal TSs, from which the diverging reaction path leads to multiple products. In reactions involving an ambimodal TS, the reaction dynamics can significantly affect the branching ratio of the products.[13,14] Recently, Tsutsumi et al.[15] proposed the idea of mapping on-the-fly MD trajectories on the reaction route map. They applied this idea to the isomerization reaction of Au_5 clusters and found "IRC jumps" corresponding to molecular transitions from one IRC to another. Furthermore, studies with reference to experiments are needed to explore the dynamical effects based on the reaction route map.

In this study, we performed automated reaction path search calculations and guided ion beam tandem mass spectrometry (GIBMS) experiments[16] for the CF_3^+ + CO reaction to validate the reaction route map with reference to experimental data. Proper data analysis of the GIBMS experimental results allows measurements of the reaction thresholds of all ionic products formed in gas-phase ion−molecule collisions,[17] which can be directly compared with the reaction route map. Note that in the CF_3^+ + CO system, the charge transfer excited state (CF_3 + CO^+) has sufficiently high energy compared to that of the ground state that one can eliminate involvement of the excited state. Nevertheless, we observe a clear discrepancy between the experimental GIBMS results and the theoretical predictions based on the reaction route map. More specifically, among the various product channels, the CF^+ + F_2CO channel is not observed experimentally even above the GRRM-predicted energy threshold of E_0 = 2.3 eV. This indicates a significant dynamical effect resulting from the non-statistical nature of the reaction dynamics. We therefore perform on-the-fly MD simulations in order to understand the experimental observations and rationalize the dynamical origins of this discrepancy.

2. RESULTS AND DISCUSSION

2.1. Guided Ion Beam Experiment and Data Analysis

Detailed descriptions of the guided ion beam apparatus used in this study and the experimental procedures are given elsewhere.[16,18] Less than 0.3% hexafluoroethane (C_2F_6, 99.999%, Matheson) mixed with 90% He and 10% Ar was supplied to a dc discharge/flow tube source[19] at a total pressure of 44 Pa and at ambient temperature. The produced CF_3^+ ions underwent ~10^5 collisions with He and ~10^4 collisions with Ar in a meter-long flow tube. Subsequently, they were mass-selected, decelerated to a desired kinetic energy, and focused into an octopole ion guide[16,20] that radially trapped the ions using radiofrequency electric fields. While in the octopole, the ions passed through a static gas cell that contained CO or N_2 at a pressure less than 0.02 Pa to ensure that multiple ion−molecule collisions did not occur. This was verified by examining the pressure dependence of the reaction cross-sections in the range of 0.007−0.02 Pa. The remaining reactant and product ions were confined in the radial direction in the guide until they drifted to the end of the octopole where they were extracted and focused into a quadrupole mass filter for mass analysis. The ions were then detected using a secondary electron scintillation ion detector,[21] and the signal was processed using standard pulse counting techniques. After correcting for background signals, ion intensities were converted to absolute reaction cross-sections, as described previously.[16] The uncertainties in absolute cross-sections were estimated to be ±20%.

The kinetic energy was varied in the laboratory frame by scanning the dc bias on the octopole rods with regard to the potential of the ion source region. Translational energies in the laboratory frame of reference are related to energies in the center-of-mass (CM) frame using $E_{CM} = E_{lab}\, m/(M + m)$, where M and m are the masses of the incident ion and neutral reactants, respectively. The kinetic energy distribution of the reactant ions and the thermal motion of the neutral reactant gas (Doppler broadening) both contributed to broadening of the cross-sections.[22,23] The octopole beam guide was used as a retarding potential analyzer, as described previously,[16] to determine both the absolute zero of the energy scale and the full width at half-maximum (fwhm) of the kinetic energy distribution of the ions. This distribution was nearly Gaussian and independent of energy, with a fwhm of 0.05−0.12 eV (CM). Uncertainties in the absolute energy scale are ±0.02 eV (CM).

The energy dependence and thresholds for the endothermic reactions were analyzed in the following way. Theory and experiments[17,24,25] show that cross-sections can be parameterized in the threshold region using

$$\sigma(E) = \sigma_0 \sum g_i (E + E_i - E_0)^n / E \quad (1)$$

where the sum is over all rovibrational states of the reactants denoted by i, g_i is the population of these states ($\Sigma g_i = 1$), E_i is the excitation energy of each rovibrational state of the reactants, σ_0 is an energy-independent scaling factor, E is the relative (CM) translational energy of the reactants, E_0 is the 0 K threshold for reaction of the ground rovibrational and electronic state of the reactants, and n is an adjustable parameter. In the absence of evidence to the contrary, it is assumed that n and σ_0 are the same for all reactant rovibrational states. Before comparison with the data, the model of eq 1 is convolved with the kinetic energy distributions of the reactants, as described previously.[16] This form is expected to be appropriate for translationally driven reactions[24] and has been found to reproduce the cross-sections for endothermic reactions in a number of previous studies of both atom−diatom and polyatomic reactions.[26−28]

Figure 1 shows the cross-sections as a function of the collision energy for reactions of CF_3^+ with both CO and N_2. Note that a supplementary experiment for the CF_3^+ + N_2 reaction was carried out to investigate the origin of the products observed in the CF_3^+ + CO reaction. The curves in the figure are the models of eq 1 with the resulting optimized parameters summarized in Table 1. In the CF_3^+ + CO collision, FCO^+, CF_2^+, and CF^+ were observed, whereas CF_2^+ was the only product ion observed in the CF_3^+ + N_2 collision. In the latter reaction, the presence of CF^+ was carefully looked for but could not be observed.

The threshold energies obtained from the CO system can be compared with the known literature thermochemistry[29,30] for the following possible reactions.

$$CF_3^+ + CO \rightarrow FCO^+ + CF_2 \qquad \Delta H_0 = 2.44 \pm 0.01 \text{ eV} \quad (2)$$

$$\rightarrow CF_2^+ + FCO \qquad \Delta H_0 = 4.52 \pm 0.01 \text{ eV} \quad (3a)$$

$$\rightarrow CF_2^+ + F + CO \qquad \Delta H_0 = 5.97 \pm 0.01 \text{ eV} \quad (3b)$$

$$\rightarrow CF^+ + F_2CO \qquad \Delta H_0 = 2.31 \pm 0.01 \text{ eV} \quad (4a)$$

https://doi.org/10.1021/acsphyschemau.2c00012
ACS Phys. Chem Au XXXX, XXX, XXX−XXX

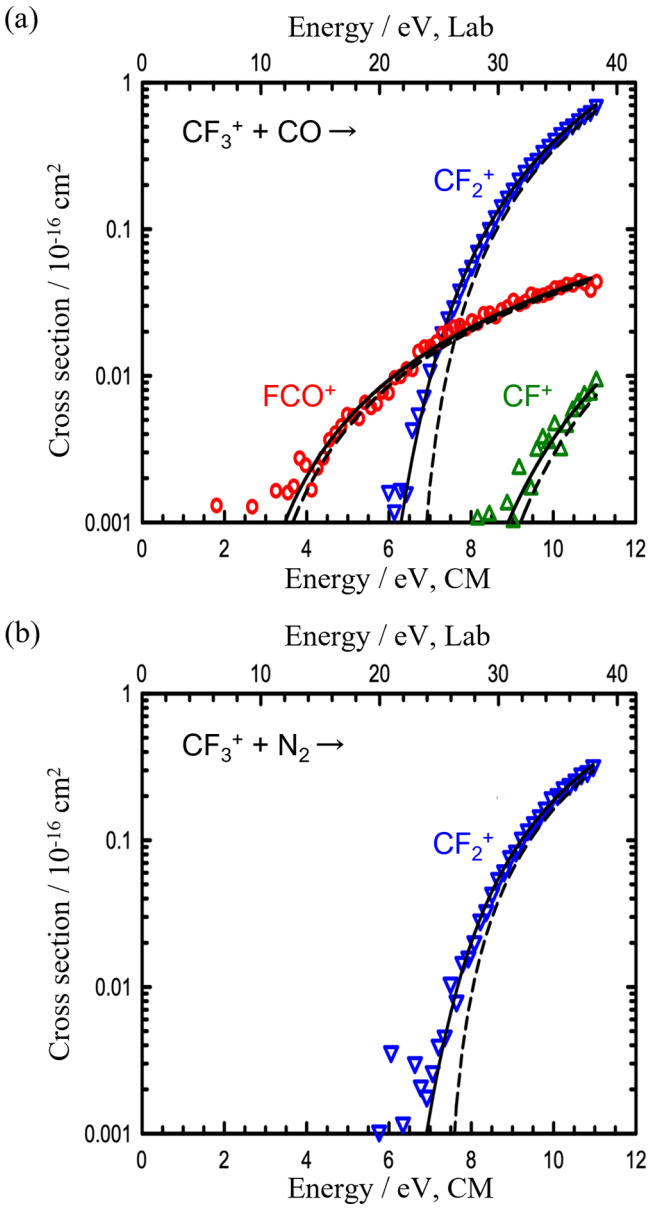

Figure 1. Cross-sections for the CF_3^+ + CO (part a) and N_2 (part b) reactions as a function of collision energy in the CM frame (lower *x*-axis) and laboratory frame (upper *x*-axis). Symbols indicate the experimental results. Solid (dashed) lines show their model cross-sections obtained using eq 1 with (without) convolution over the kinetic and internal energy distributions of the reactants.

Table 1. Optimized Parameters for eq 1 for the CF_3^+ + CO and N_2 Reactions[a]

reactants	product ions	n	σ_0	E_0/eV
CF_3^+ + CO	FCO^+	2.9 ± 0.2	0.0015 ± 0.0002	2.39 ± 0.05
	CF_2^+	2.8 ± 0.2	0.10 ± 0.02	6.40 ± 0.20
	CF^+	3.0 ± 0.2	0.0018 ± 0.0003	7.48 ± 0.15
CF_3^+ + N_2	CF_2^+	2.3 ± 0.1	0.18 ± 0.02	7.35 ± 0.11

[a]Uncertainties are one standard deviation.

$$\rightarrow CF^+ + F + FCO \qquad \Delta H_0 = 7.54 \pm 0.01 \text{ eV} \qquad (4b)$$

$$\rightarrow CF^+ + F_2 + CO \qquad \Delta H_0 = 7.39 \pm 0.01 \text{ eV} \qquad (4c)$$

$$\rightarrow CF^+ + 2F + CO \qquad \Delta H_0 = 8.99 \pm 0.01 \text{ eV} \qquad (4d)$$

It can be seen that the measured threshold for generation of FCO^+ is in good agreement with the 0 K energy needed for reaction 2; hence, this reaction clearly corresponds to the transfer of F^+ from CF_3^+ to CO. The complementary channel in which the charges of the two products are exchanged, reaction 3a, is much lower in energy than the observed threshold for CF_2^+ formation. Here, it can also be realized that reaction 2 corresponds to heterolytic bond cleavage of a $[FCO{-}CF_2]^+$ intermediate. As a consequence, the alternative CF_2^+ + FCO asymptote, the homolytic bond cleavage, actually correlates with an unstable excited state (triplet or singlet spin) of the same intermediate.[31] Hence, experimental formation of CF_2^+ appears to correspond to the collision-induced dissociation (CID) reaction 3b, consistent with the similarity with the reaction of CF_3^+ with N_2, Figure 1. We believe that the difference in the thresholds obtained for these two CID reactions can be traced to a stronger interaction with CO, which allows more efficient energy transfer. The observation of reaction 2 is clear evidence for this stronger interaction.

Four possible reactions are available to generate CF^+ with the literature thermochemistry for reaction 4a lying much lower than the observed threshold energy. In contrast, reactions 4b and 4c are consistent with the observed threshold energy, whereas the enthalpy of reaction 4d lies too high to explain the experimental observations. Note that reaction 4d corresponds to the subsequent dissociation of an initially formed CF_2^+ product in reaction 3b. The experiment suggests that the observation of CF^+ probably corresponds to reaction 4c because reaction 4b must be preceded by either reactions 3a or 4a, neither of which is obviously observed in the experiment. The failure to see CF^+ in the reaction with N_2 indicates that the CID reaction 4c is also not expected to occur in the collision reaction between CF_3^+ and CO; however, given the relative magnitudes of the cross-sections for CF_2^+ (about half as large in the N_2 system), it is possible that observation of CF^+ in reactions with N_2 was near the noise level. It is also possible that CF^+ is formed in reaction 4a with a threshold shifted to high energies by a barrier or dynamic constraints. Thus, it is difficult to clarify the collision energy dependence of the reaction mechanism from experimental studies alone.

2.2. Reaction Route Map for CF_3^+ + CO

To understand the reaction mechanism for the reaction of CF_3^+ and CO investigated by the GIBMS experiment, we carried out automated reaction path search calculations by employing the ADDF method[3,4] at the UB3LYP/6-31+G(d) level with singlet spin multiplicity. The stable = opt[32,33] option was specified to describe the doublet−doublet dissociation. To verify the accuracy of the computed reaction route map, we performed geometry optimization of the stationary points using the aug-cc-pVTZ basis set at the coupled-cluster single, double, and perturbative triple [CCSD(T)] level (see S1 in Supporting Information). Consequently, we confirmed that the UB3LYP results are in qualitative agreement with the CCSD(T) results with a root mean square error of 0.15 eV. More importantly, comparison of the UB3LYP/6-31+G(d) theoretical results with the literature thermochemistry shown in reactions 2−3b shows deviations of less than 0.2 eV for all five product asymptotes, with a mean absolute deviation of 0.12 ± 0.07 eV. The energy of the dissociation products was calculated as the sum of the energies of the isolated fragments. The electronic structure

https://doi.org/10.1021/acsphyschemau.2c00012
ACS Phys. Chem Au XXXX, XXX, XXX−XXX

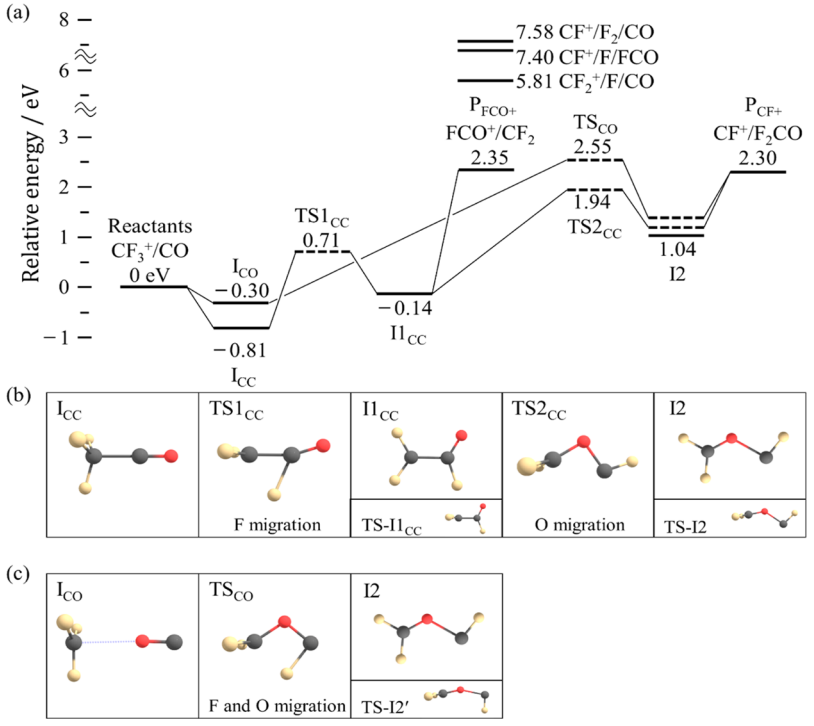

Figure 2. (a) Energy diagram of the CF_3^+ + CO reaction determined from the reaction route map at the UB3LYP/6-31+G(d) level. Energies are given in eV relative to the reactants. The equilibrium structures and the TS structures are depicted by solid and dashed lines, respectively. (b) Structural change from I_{CC} to $I1_{CC}$ via $TS1_{CC}$ and from $I1_{CC}$ to I2 via $TS2_{CC}$. (c) Structural change from I_{CO} to I2 via TS_{CO}. Note that the dashed line for TS-$I1_{CC}$ (−0.11 eV) is too close to the line for $I1_{CC}$ (−0.14 eV) to be displayed.

calculations were performed using Gaussian09 Revision D.01,[34] and the ADDF calculations were performed using GRRM14.[35]

The ADDF calculations yielded 172 equilibrium structures, 417 TS structures, and 66 dissociation structures for the CF_3^+/CO collision reaction. From these structures, we extracted low-energy regions that are relevant to the experimental observations. Figure 2a shows the energy diagram of the stationary points along the reaction paths from the CF_3^+/CO reactants to the low-energy dissociation channels FCO^+/CF_2 (denoted as P_{FCO+}) and CF^+/F_2CO (denoted as P_{CF+}). The calculated energies of the high-energy channels containing the ions observed in the experiment, CF_2^+/F/CO, CF^+/F/FCO, and CF^+/F_2/CO, are also shown. The initial interaction of CF_3^+ and CO reactants leads to the formation of two complexes, $[F_3C{-}CO]^+$ (I_{CC}) and $[F_3C{-}OC]^+$ (I_{CO}). The structures of I_{CC} and I_{CO} are shown in Figures 2b and c, respectively. In addition, Figure 2a shows the energies of the relevant TSs ($TS1_{CC}$, $TS2_{CC}$, and TS_{CO}) and the planar structure intermediates, $[F_2CCFO]^+$ ($I1_{CC}$) and $[F_2COCF]^+$ (I2), that lie on the reaction path from the complex I_{CC} or the complex I_{CO} to the dissociation products. In addition, Figures 2b and c shows three TS structures TS-$I1_{CC}$ (−0.11 eV), TS-I2 (1.20 eV), and TS-I2′ (1.39 eV) as auxiliary TSs leading to the planar intermediates of interest. As shown, intermediates $I1_{CC}$ and I2 are planar versions of TS-$I1_{CC}$ and TS-I2, respectively. Our calculations indicate that TS-$I1_{CC}$ corresponds to the TS of CF_2 rotation of the complex $I1_{CC}$ (−0.14 eV). Similarly, TS-I2 and TS-I2′ correspond to the TSs of CF_2 rotation of the intermediate I2 (1.04 eV). According to the IRC calculations, $TS1_{CC}$ is connected to the TS-$I1_{CC}$, whereas $TS2_{CC}$ is connected to TS-$I1_{CC}$ and TS-I2, and TS_{CO} is connected to TS-I2′. Note that the connection of TSs such as $TS1_{CC}$ and TS-$I1_{CC}$ indicates the appearance of a valley−ridge inflection point[2] along the IRC.

We now summarize the key structural changes that are predicted to occur along the various pathways leading to the different product channels. Figure 2b shows the structural change from I_{CC} to I2. Upon isomerization, the complex I_{CC} isomerizes to $I1_{CC}$ via $TS1_{CC}$ with the migration of a F atom, and the system proceeds along the P_{FCO+} channel to produce FCO^+ by C−C bond cleavage over a loose TS. Alternatively, the system can further isomerize to I2 via $TS2_{CC}$ with the migration of an O atom to produce CF^+ by C−O bond cleavage over a loose TS. In contrast, Figure 2c shows the structural change from I_{CO} to I2 after the simultaneous migration of F and O atoms via TS_{CO}. We note that the reaction paths for the dissociation of $I1_{CC}$ to FCO^+ via the P_{FCO+} channel and from I2 to CF^+ via the P_{CF+} channel are uphill, and there is no tight TS. We also found the TS structure of the reaction path in which CF_3^+ and CO collide from the F-atom side ($F_2C{-}F{\cdots}CO$), leading to P_{CF+}; however, the activation barrier for this path is significantly higher (3.56 eV) than that of the $I_{CC} \rightarrow TS1_{CC} \rightarrow I1_{CC} \rightarrow TS2_{CC} \rightarrow$ I2 $\rightarrow P_{CF+}$ pathway. Therefore, we do not consider the collision from CO to the F-atom side in the following discussion.

As shown in the previous section (cf. Figure 1 and Table 1), the energy thresholds for the product ions obtained from the GIBMS experiments are 2.39 ± 0.05 eV for FCO^+, 6.40 ± 0.20 eV for CF_2^+, and 7.48 ± 0.15 eV for CF^+. In comparison, the ADDF calculations show that the relevant thresholds are 2.35 eV for FCO^+/CF_2, 5.81 eV for CF_2^+/F/CO, and 2.30 eV for CF^+/F_2CO. Thus, the ADDF results are in relatively good agreement with the GIBMS results for the FCO^+/CF_2 and CF_2^+/F/CO product channels. However, and perhaps surprisingly, there is a large difference between the GIBMS-observed and ADDF-predicted threshold for the CF^+ channel. In this regard, it can be realized that the intermediate $I1_{CC}$ can undergo further reaction either by dissociation over the loose TS leading to FCO^+/CF_2

https://doi.org/10.1021/acsphyschemau.2c00012
ACS Phys. Chem Au XXXX, XXX, XXX−XXX

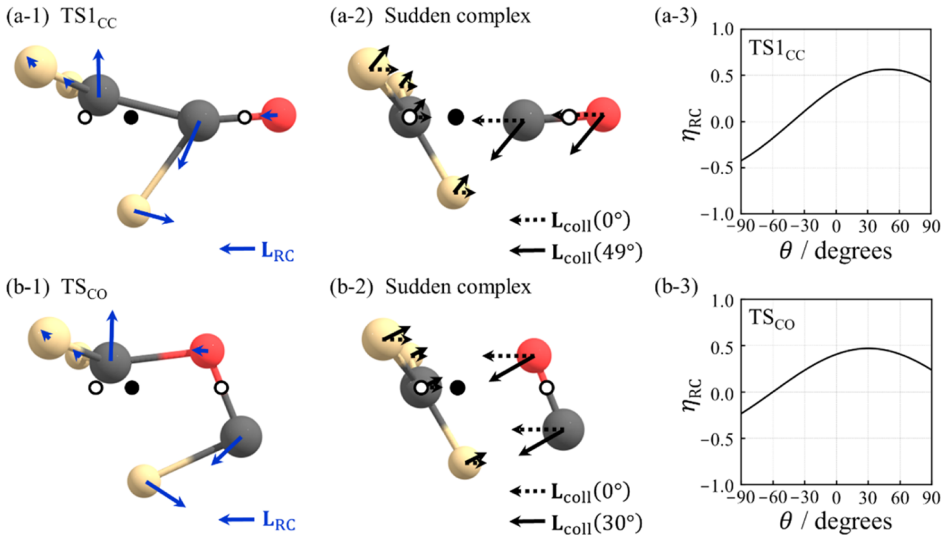

Figure 3. (a-1) Structure of $TS1_{CC}$ in $F_3C^+\cdots CO$ collisions, (a-2) the structure of the corresponding sudden complex, and (a-3) SVP-based parameter $\eta_{RC}(\theta)$ as a function of collision angle; (b-1) structure of TS_{CO} in $F_3C^+\cdots OC$ collisions, (b-2) structure of the corresponding sudden complex, and (b-3) SVP-based parameter $\eta_{RC}(\theta)$ as a function of collision angle. The RC mode $\mathbf{L}_{RC}$ at the TS and the collision mode $\mathbf{L}_{coll}$ at the sudden complex are indicated by arrows in each panel. In each molecular structure, the solid circle and the open circle indicate the center of mass of the entire molecular system and the center of masses of the reactant molecules, respectively.

(at 2.35 eV) or by passing over $TS2_{CC}$ (at 1.94 eV) followed by dissociation to CF^+/F_2CO (at 2.30 eV). Because the overall energetics are similar, the dissociation to FCO^+/CF_2 will be favored because it does not require passing over the entropically disfavored tight $TS2_{CC}$. Higher energy dissociation channels producing CF^+ include $CF^+/F/FCO$ and $CF^+/F_2/CO$, with relative energies calculated to be 7.40 and 7.58 eV, respectively (cf. Figure 2a). These values quantitatively agree with the experimentally observed threshold for CF^+ shown in Table 1. The same experiment was also performed for the collision of CF_3^+/N_2 as shown in Figure 1b, where CF_2^+ was observed as the only product. It can be seen that the energy behavior of CF_2^+ is similar in both systems. This comparison indicates that CF_2^+ originates from the CID of CF_3^+ with CO (or N_2), whereas FCO^+ originates from more complicated rearrangements in the reaction of CF_3^+ with CO. Because of its high energy, the reaction associated with the CF^+ product is not completely clear, as noted above. As described above, for reaction 4a, there is an apparent discrepancy between the reaction route map that predicts the pathway for the formation of CF^+/F_2CO and the GIBMS experiment.

2.3. On-the-Fly MD for CF_3^+ + CO

2.3.1 Initial Conditions for Promoting the Collision Reaction. In order to resolve the discrepancy between the GIBMS experiment and the reaction route map and to gain a better understanding of the reaction dynamics, we performed on-the-fly MD simulations for the CF_3^+ + CO reaction. First, we ran 100 trajectories under random initial conditions and found that the colliding molecules passed each other, and no chemical reaction occurred. This result is reasonable considering that the reaction cross-section is very small (less than 0.01 $Å^2$ at 5 eV collision energy), as shown in Figure 1. This magnitude is about 1000 times smaller than other collision reactions studied in MD simulations.[36,37] Therefore, the dynamics simulation of this collision reaction requires an efficient selection of the initial conditions for the chemical reaction to occur.

In ion−molecule reactions, a pre-reaction complex is usually formed by the reactants. Previous experimental and theoretical studies have shown that when the translational energy of the reactant molecules is relatively high, most of the trajectories are not trapped in the pre-reaction complex and can directly reach the TS region.[38−41] In such bimolecular reactions with direct collision processes, the sudden vector projection (SVP) model proposed by Jiang and Guo provides a good approximation to elucidate the reaction mechanism.[42] Assuming a direct collision mechanism, the reactant molecules will probably collide in the same relative orientation as the TS during any collision that leads to products. In the SVP model, the reactant molecules are placed in this relative orientation, and the inner product between the basis vectors of the translational, rotational, and vibrational modes of the reactant molecules and the reaction-coordinate (RC) mode at the TS is calculated to estimate the effect of each mode in promoting the reaction. This model was proposed by generalizing Polanyi's rule,[43] which is well known for atom−diatom collisions, to polyatomic bimolecular reactions.[44−46]

In the CF_3^+/CO system, the reaction route map shows that a collision energy of at least 2.3 eV is required to reach CF^+/F_2CO. If the reactant molecules have enough translational energy to reach the P_{CF+} channel upon collision, the reactants are expected to reach the initial TS directly without being trapped in the pre-reaction complex. Of course, in GIBMS experiments, the relative orientation of the reactant molecules may change before reaching this TS because of molecular vibrations or rotational motion, but here, we assume a direct collision mechanism that leads to the vicinity of the TS without changing the orientation. Here, we consider the two TSs that correspond to the first TS of the reactions leading to P_{CF+}. CF_3^+ + CO reactions can occur via $TS1_{CC}$ or TS_{CO} and are assumed to occur via a relative orientation similar to the structure of the optimized TS. This assumption allows for proper sampling that defines the initial collision conditions to obtain the reactive trajectories.

First, we define the ideal atomic coordinates of the reactant molecules just before the collision. Reactant molecules are placed in mass-weighted Cartesian coordinates to maximize their structural overlap with the TS geometry using the Kabsch algorithm,[47] keeping the center of mass of each reactant

https://doi.org/10.1021/acsphyschemau.2c00012
ACS Phys. Chem Au XXXX, XXX, XXX−XXX

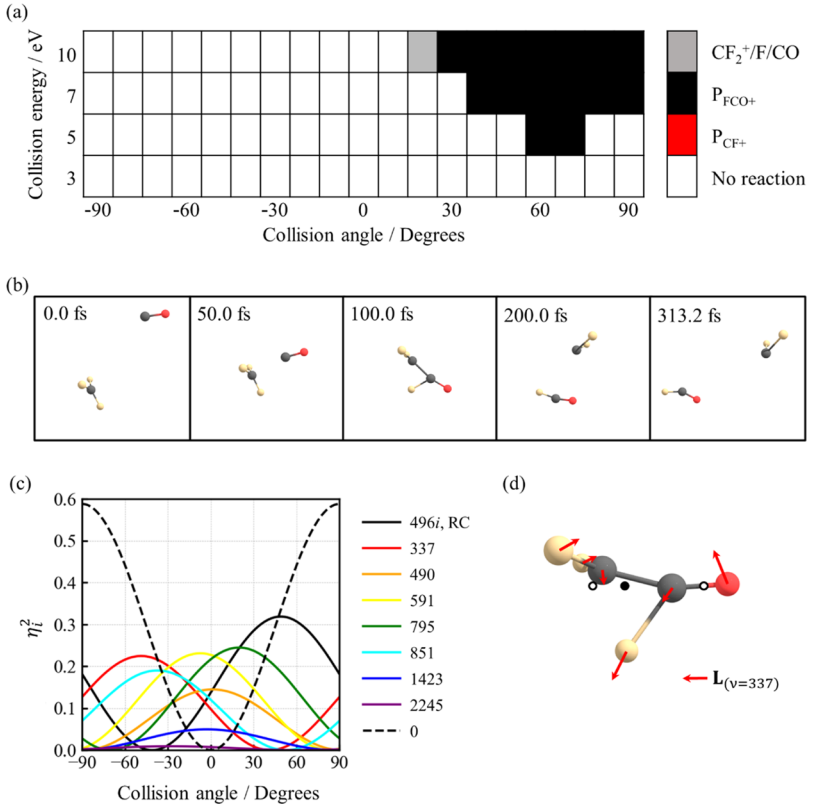

Figure 4. (a) Heat map of the 76 trajectory termination structures in the case of $F_3C^+\cdots CO$ collisions. (b) Snapshots of the molecular geometry along the trajectory resulting in P_{FCO+} calculated for $\theta = 70°$ and $E_{coll} = 5$ eV. (c) Variation of η_i^2 calculated for the collision mode and ith normal mode at $TS1_{CC}$ as a function of collision angle from −90° to 90°. The number written next to each line indicates the corresponding mode vibrational frequency in cm^{-1} (0 corresponds to the rotational mode that preserves C_s symmetry). (d) Oxygen migration mode $\mathbf{L}_1$ (ν_1 = 337 cm^{-1}) at $TS1_{CC}$, which is essential for reaching $TS2_{CC}$.

molecule fixed at the corresponding position in the TS geometry. We call this structure a sudden complex in which the reactant molecules suddenly approach the TS region without changing their respective geometries. Figure 3 shows the geometry of $TS1_{CC}$, the corresponding sudden complex for $F_3C^+\cdots CO$ collisions, the geometry of the TS_{CO}, and the corresponding sudden complex for $F_3C^+\cdots OC$ collisions. Note that the center of mass of the entire molecular system is located on the line connecting the centers of mass of the reactants (hereafter referred to as the collision line).

Next, we introduce the collision mode $\mathbf{L}_{coll}$, which is represented by a linear combination of the translational modes of each of the reacting molecules superimposed so that they approach each other. In the collision mode, the center of mass of the entire system is fixed at the origin, so the kinetic energy given in this mode corresponds to the collision energy in the CM frame. Consider the case where the motion of the atoms in the reactant molecules determined in the collision mode is parallel to the collision line. The collision mode obtained by rotating the translational mode of each reactant molecule by an angle θ (called the collision angle) counterclockwise in the C_s symmetry plane with respect to the collision line is called $\mathbf{L}_{coll}(\theta)$.

Furthermore, we introduce the SVP-based parameter $\eta_{RC}(\theta) = \mathbf{L}_{coll}(\theta)\cdot\mathbf{L}_{RC} \in [0,1]$, which is the inner product of the collision mode $\mathbf{L}_{coll}$ and the RC mode $\mathbf{L}_{RC}$ at a TS, as an index to evaluate how efficiently the collisional momenta contribute to the crossing of the specific TS of interest. The optimal collision angle θ^{opt} that maximizes η_{RC} allows the molecular system to traverse the TS region in the most efficient way. Figures 3a-3 and b-3 show $\eta_{RC}(\theta)$ as a function of collision angle in the range of $-90° \leq \theta \leq 90°$ for $TS1_{CC}$ and TS_{CO}, respectively. The maximum $\eta_{RC}(\theta)$ is 0.56 ($\theta^{opt} = 49°$) for $TS1_{CC}$ and 0.47 ($\theta^{opt} = 30°$) for TS_{CO}. In Figures 3a-2 and b-2, the collision modes with collision angles $\theta = 0°$ and θ^{opt} for the sudden complexes are indicated by arrows. The collision mode with the optimal collision angle is in relatively good agreement with the RC mode in Figures 3a-1 and b-1.

2.3.2 Trajectories for the $F_3C^+\cdots CO$ Collision. On the basis of the SVP analysis described in the previous section, initial conditions were prepared by separating the reactant molecules by 5 Å along the collision mode $\mathbf{L}_{coll}(\theta)$ from the sudden complex structure of interest at 19 collision angles of $\theta = -90°$, −80°, ..., and 90°. In addition, the initial momenta along the collision mode corresponding to four different collision energies (E_{coll}) of 3, 5, 7, and 10 eV were considered. Starting from these 76 initial conditions for $F_3C^+\cdots CO$ collisions, we performed on-the-fly MD calculations at the UB3LYP/6-31+G(d) level using the in-house program SPPR[48] linked to Gaussian09.[34] We considered the case of singlet spin multiplicity for the entire molecular system and used the stable = opt option[32,33] to deal with dissociation in open-shell electron configurations. The velocity-Verlet algorithm[49] was used for the time evolution of Newton's equation of motion, with a time step of 0.4 fs. The calculation for each trajectory was stopped when the C···C distance exceeded 6 Å.

Figure 4a shows a heat map of the 76 trajectory termination structures for $F_3C^+\cdots CO$ collisions. The product FCO^+ (threshold energy = 2.35 eV) was observed only at collision

https://doi.org/10.1021/acsphyschemau.2c00012
ACS Phys. Chem Au XXXX, XXX, XXX−XXX

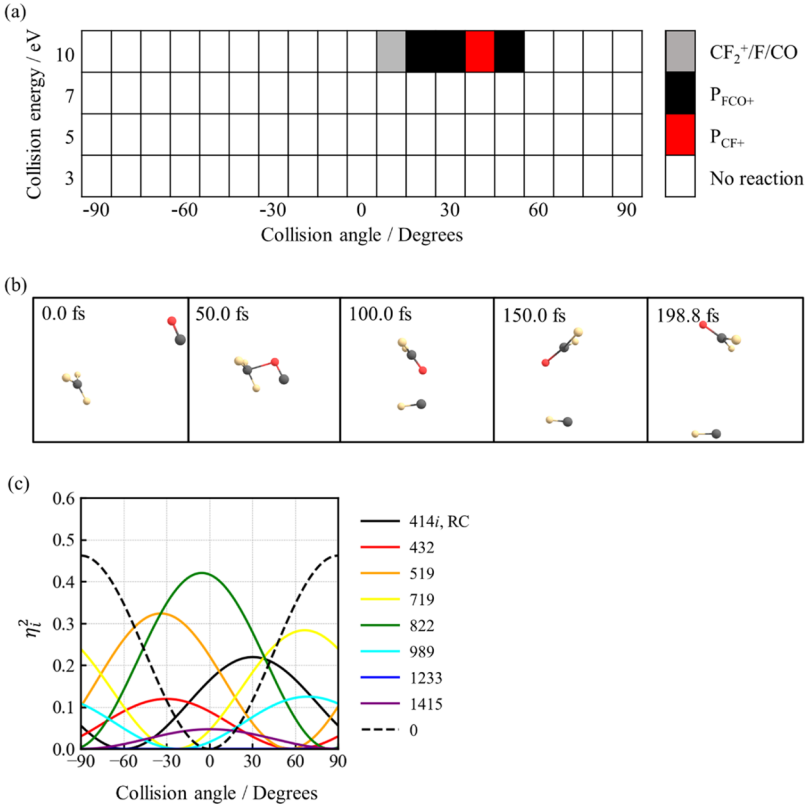

Figure 5. (a) Heat map of the 76 trajectory termination structures in the case of $F_3C^+\cdots OC$ collisions. (b) Snapshots of the molecular geometry along the trajectory resulting in P_{CF+} calculated for $\theta = 40°$ and $E_{coll} = 10$ eV. (c) Variation of η_i^2 calculated for the collision mode and ith normal mode at TS_{CO} as a function of the collision angle from −90° to 90°. The number written next to each line means the vibrational frequency in cm^{-1} (0 corresponds to the rotational mode which preserves C_s symmetry).

angles close to the optimum one, 49°. As collision energy increases, the collision angles leading to the product FCO^+ become more dispersed. The product from the collision with θ = 20° and E_{coll} = 10 eV was assigned to a product of three-body dissociation (CF_2^+/F/CO). Note that the P_{CF+} channel is not observed in any of the trajectories, which is consistent with the GIBMS experiment.

Before going into a detailed analysis of the dynamics, we mention additional simulations (see S2 in Supporting Information) that were performed to validate the restrictions we imposed on the atomic coordinates of the reactant molecules. In these additional simulations, the initial coordinates of the atoms were generated anew by rotating the reactant molecules in 30° increases from −90° to 90° around the CM point in the C_s symmetry plane to change their relative orientation. At collision angles θ = 60° and 70°, corresponding to a majority of the reactive trajectories in Figure 4a, on-the-fly MD simulations were performed again for these new initial coordinates and for several collision energies. The results showed that some trajectories with slightly altered initial coordinates undergo chemical reactions, whereas other trajectories show non-reactive collisions. This result supports the assumption that the CF_3^+/CO reaction occurs at least through the direct collision process via the atomic coordinates near the sudden complex.

Figure 4b shows a snapshot of the structural change of the reactive trajectories starting from θ = 70° and E_{coll} = 5 eV as an example. From this figure, we can understand how one fluorine atom moves between a molecule and a dissociating fragment. In this case, there is not enough time for intramolecular vibrational energy redistribution (IVR) to occur around $TS\text{-}I1_{CC}$, where CO associates with CF_3^+, so CO smoothly removes F^+ and proceeds to the dissociation channel P_{FCO+}. The fate of the trajectory after crossing $TS1_{CC}$ depends on the energy distribution to the molecular degrees of freedom at $TS1_{CC}$. In order to understand why this reaction system reaches the product P_{FCO+} and not $TS2_{CC}$, it will be important to consider the very fast intramolecular energy redistribution that occurs during the process of reaching $TS1_{CC}$ through molecular collisions.

We now extend the SVP analysis to modes other than the RC mode and introduce $\eta_i(\theta) = \mathbf{L}_i \cdot \mathbf{L}_{coll}(\theta)$, where $\mathbf{L}_i$ is the ith normal mode of the reactive molecular system defined for the TS structure and represents one of the RC modes, vibrational modes, and rotational modes that preserve C_s symmetry. In the present analysis, we use the squared value, $\eta_i(\theta)^2$, to estimate how the collision energy is distributed among the molecular degrees of freedom after the molecular system passes near the TS structure (see S3 in Supporting Information for details). As shown in Figure 4c, the black dashed line corresponding to the rotational mode with frequency 0 cm^{-1} shows a relatively large value compared to other modes around the collision angle of 50° where the RC mode shows its maximum, and this rotational mode is expected to be excited at this collision angle. In fact, the snapshot in Figure 4b shows that CO moving downward collides with CF_3^+ at around 100 fs, leading to the TS structure, and after receiving one F atom, it changes its direction of motion to the left by rotational motion and dissociates. This result suggests that the analysis using $\eta_i(\theta)^2$ is effective in predicting the energy redistribution associated with the collision.

https://doi.org/10.1021/acsphyschemau.2c00012
ACS Phys. Chem Au XXXX, XXX, XXX−XXX

According to the reaction diagram in Figure 2, in order to reach the P_{CF+} region, the molecular system needs to cross $TS1_{CC}$ and then reach $TS2_{CC}$, which requires oxygen atoms to move between the two carbon atoms. The vibrational mode $\mathbf{L}_1$ at $TS1_{CC}$ shown in Figure 4d corresponds to such a movement of the oxygen atom. In fact, we performed a preliminary calculation of on-the-fly MD by starting from $TS1_{CC}$ and giving large kinetic energy in the direction of $\mathbf{L}_1$ and confirmed that some trajectories reach $TS2_{CC}$. However, as shown in Figure 4c, η_1^2 is small when the collision angle is around $\theta^{opt} = 49°$, which means that energy will not flow into the vibrational mode leading to $TS2_{CC}$, and the reaction leading to P_{CF+} production will not occur. On the other hand, when the collision angle is between −45° and −30°, the η_1^2 is relatively large and the molecular system may reach $TS2_{CC}$ after crossing $TS1_{CC}$, but the η_{RC}^2 is small and the collision energy must be quite large for the molecular system to pass $TS1_{CC}$ (the interpretation of η_{RC}^2 will be explained in the next section). Note that, with the collision angle being more negative than about −45°, the reactants cannot reach $TS1_{CC}$ because η_{RC} is negative, as shown in Figure 3a-3. As a result, at low collision energies, molecular systems are not expected to pass through $TS1_{CC}$ and $TS2_{CC}$ to produce CF^+ via the P_{CF+} channel. This phenomenon, in which the momentum at the TS determines the outcome of the product, is called "dynamic matching" and has attracted much attention in the study of the dynamics of organic reactions.[50,51]

We also calculated trajectories with collision angles near the optimum angle and collision energies of E_{coll} = 3.5, 4.0, and 4.5 eV, but no reaction occurred in any of the cases. In addition, we generated trajectories using 600 different initial conditions with zero-point vibrational energies in all the vibrational modes along with relatively small collision energies and found trajectories that followed the P_{FCO+} channel but not the P_{CF+} channel. The details can be found in Supporting Information (S4). Note that the initial conditions for a number of the on-the-fly MD calculations performed here were limited to collision conditions so that the $FCO^+ + CF_2$ channel could be realized. No simulations were performed specifically for the CID reaction in which energy is just transferred to the internal energy of CF_3^+ and bond dissociation occurs. Nevertheless, as shown in Figure 4a, dissociation to $CF_2^+ + F$ which corresponds to the CID reaction was observed. Because CID does not require a specific reactant orientation to transfer energy from translation into internal degrees of freedom, it is clear that many collisions would lead to this process, consistent with the relatively larger magnitudes of the CF_2^+ cross-sections compared to those for FCO^+ in Figure 1.

2.3.3 Trajectories for the $F_3C^+\cdots OC$ Collision. We also performed on-the-fly MD simulations for $F_3C^+\cdots OC$ collisions, in which CO collides with F_3C^+ from the O atom side, using the same procedure as for $F_3C^+\cdots CO$ collisions. Figure 5a shows the heat map of the 76 trajectory-terminated structures: the relative energy of TS_{CO} is 2.55 eV, but the reaction only occurs at E_{coll} = 10 eV, the maximum collision energy considered in the present study. As in the case of $F_3C^+\cdots CO$ collisions, the reaction occurred near the corresponding optimal collision angle of θ^{opt} = 30°. Surprisingly, the dominant product was P_{FCO+} ($FCO^+ + CF_2$), which can be formed starting at the structure of TS_{CO} because the directions of the velocity vectors can lead to this thermodynamically favored process. Note that in the reactive trajectory with collision angle θ = 40°, CF^+ was produced (Figure 5b). This result suggests that the CF^+ observed starting at a collision energy of 7.48 eV in the GIBMS experiment may be produced not only in the three-body dissociation channel $CF^+/F_2/CO$, reaction 4c, but also in the P_{CF+} (CF^+/F_2CO) channel, reaction 4a.

The reason as to why it takes significantly more energy than the height of the barrier to cross TS_{CO} can be understood by considering the value of $\eta_{RC}(\theta)^2$. In the vicinity of the TS structure, the molecular system climbs the PES along the direction of the RC mode. Therefore, the collision energy in the RC direction is used to cross the TS. Here, $\eta_{RC}(\theta)^2$ represents the relative ratio of the effective energy allocated to the RC direction out of the collision energy. Of course, this interpretation is valid only in the very near vicinity of the TS structure, and in the actual chemical reaction, the collision energy in the RC direction can be distributed to the various degrees of freedom in the molecular system. Therefore, the values obtained here should be regarded as qualitative or semi-quantitative.

In the $F_3C^+\cdots OC$ collision reaction via TS_{CO}, the maximum value of η_{RC}^2 is 0.22 (Figure 5c), which means that within the SVP model, less than a quarter of the collision energy contributes to the motion along the RC mode. In other words, if the SVP model is strictly applied, even if the collision energy is 10 eV, the effective energy available for the reaction (10 eV × 0.22 = 2.2 eV) is less than the TS_{CO} barrier height of 2.55 eV. Therefore, significantly higher collision energies are required to efficiently access and cross the TS_{CO} transition state. It has been reported in previous trajectory studies that the collision energy is not always effective in assisting the reaction.[52,53] Note that the estimation scheme based on the SVP model is too simple to quantitatively evaluate an effective energy. Actually, the CF^+ ion observed in the GIBMS experiment, which could originate from the CF^+/F_2CO channel, shows a threshold of 7.48 ± 0.15 eV which is significantly lower than 10 eV. Nevertheless, such an estimate provides a qualitative understanding for the different energetic behavior associated with the P_{FCO+} or P_{CF+} channels. Unlike the P_{CF+} case, formation of FCO^+ via the P_{FCO+} channel requires crossing of $TS1_{CC}$ with a barrier height of 0.71 eV. The corresponding maximum η_{RC}^2 value of 0.33 in the case of $F_3C^+\cdots CO$ collisions (Figure 4c) therefore requires a minimum energy of (0.71 eV /0.33 =) 2.15 eV, which is below the required asymptotic energy of 2.35 eV. Thus, our analysis based on η_{RC}^2 explains the correspondence between the observed and calculated energetics for this channel.

3. CONCLUSIONS

In quantum chemical studies of chemical reactions, the IRC plays an important role in elucidating the reaction mechanism. The automated reaction path search methods have made it possible to determine the IRC network (the reaction route map) on the PES and to reveal the reaction mechanism without any assumptions. On the other hand, some studies have pointed out that the true reaction mechanism may differ from the one inferred from the reaction path picture because of dynamical effects caused by the atomic momenta of the molecular system. It is therefore important that such dynamical effects on the reaction route map be investigated with reference to experiments.

In this study, we performed GIBMS experiments and automated reaction path search calculations for the $CF_3^+ + CO$ reaction. The formation of FCO^+ and CF_2^+ can be readily explained using reactions 2 and 3b, but for the formation of CF^+, there was a discrepancy between the dissociation threshold of 7.48 ± 0.15 eV obtained from the GIBMS experiment and the energy required along the CF^+ formation pathway of 2.30 eV

https://doi.org/10.1021/acsphyschemau.2c00012
ACS Phys. Chem Au XXXX, XXX, XXX−XXX

from the theoretical calculation. This discrepancy between experimental and theoretical results suggests that the molecular system does not follow the theoretically predicted reaction path leading to $CF^+ + F_2CO$ because of dynamical effects. It is also entropically disfavored compared to the reaction path leading to $FCO^+ + CF_2$. To investigate this further, we performed on-the-fly MD simulations of the collision process between CF_3^+ and CO with the aid of the SVP model, assuming that it goes through the $TS1_{CC}$ or the TS_{CO} transition states.

From the results of the on-the-fly MD calculations, the dynamics of the CF_3^+ + CO reaction can be interpreted as follows. In the GIBMS experiment, thermalized reactant molecules (Boltzmann distributed at a certain temperature with vibrational and rotational degrees of freedom) collide with a fairly large (variable) amount of translational energy. This large collision energy causes the reactant molecules to approach the TS regions directly without being trapped by the potential minimum of the pre-reaction complex, so that the energy distribution of the internal degrees of freedom of the molecules remains unrelaxed and biased. Clearly, the energy of the molecular system after crossing the TS deviates from a statistical distribution. For this reason, the trajectory after crossing $TS1_{CC}$ cannot follow the reaction path to $TS2_{CC}$, and crossing TS_{CO} requires much higher collision energy than the reaction barrier. As a result, at low collision energies, the system cannot dissociate into $CF^+ + F_2CO$ via $TS1_{CC}$ or TS_{CO}, leading to the discrepancy in the threshold for CF^+ production between the GIBMS experiment and the predicted reaction route map.

Conventional arguments based on reaction paths obtained by quantum chemical calculations do not take into account the possibility that a molecular system with enough energy to cross the reaction barrier cannot follow the reaction path. In this study, we discovered the existence of a "dynamically hidden reaction path" in which a molecular system cannot follow the reaction path because of dynamical effects, even though the energetically accessible reaction path exists, and clarified its mechanism. Recent theoretical and experimental studies have revealed that in various reactions, such as gas-phase, condensed-phase, and gas−surface interface reactions, the energy distribution can be non-statistical because of an incomplete redistribution of intramolecular vibrational energy.[54] These observations suggest that dynamically hidden paths may be common in other reactions as well. With the advent of the concept of reaction route maps based on automated reaction path search methods, the role of reaction dynamics in determining the destination of chemical reactions will become increasingly clear.

■ ASSOCIATED CONTENT

Supporting Information

The Supporting Information is available free of charge at https://pubs.acs.org/doi/10.1021/acsphyschemau.2c00012.

Animation file for on-the-fly trajectory, non-reactive_-trajectory_CC_collision_5ev_0deg (MP4)

Reactive_trajectory_CC_collision_5ev_70deg (MP4)

Reactive_trajectory_CO_collision_10ev_40deg (MP4)

Comparison of relative energies of stationary points between UB3LYP and CCSD(T); derivation of coupling between the collision mode and normal modes at the TS; on-the-fly MD, with various initial relative orientations, with zero-point vibrational energies, from the TS to reactant; and Cartesian coordinates of some structures (PDF)

■ AUTHOR INFORMATION

Corresponding Authors

Kenji Furuya − *Faculty of Arts and Science, Kyushu University, Motooka, Fukuoka 819-0395, Japan; Department of Molecular and Material Sciences, Kyushu University, Kasuga, Fukuoka 816-8580, Japan; Department of Chemistry, University of Utah, Salt Lake City 84112, United States*; Email: furuya.kenji.261@m.kyushu-u.ac.jp

Tetsuya Taketsugu − *Department of Chemistry, Faculty of Science, Hokkaido University, Sapporo 060-0810, Japan; Institute for Chemical Reaction Design and Discovery (WPI-ICReDD), Hokkaido University, Sapporo 001-0021, Japan*; orcid.org/0000-0002-1337-6694; Email: take@sci.hokudai.ac.jp

Authors

Kohei Oda − *Graduate School of Chemical Sciences and Engineering, Hokkaido University, Sapporo 060-0810, Japan*; orcid.org/0000-0002-5684-2499

Takuro Tsutsumi − *Department of Chemistry, Faculty of Science, Hokkaido University, Sapporo 060-0810, Japan*

Srihari Keshavamurthy − *Department of Chemistry, Faculty of Science, Hokkaido University, Sapporo 060-0810, Japan; Department of Chemistry, Indian Institute of Technology, Kanpur 208 016, India*; orcid.org/0000-0002-4424-6745

P. B. Armentrout − *Department of Chemistry, University of Utah, Salt Lake City 84112, United States*; orcid.org/0000-0003-2953-6039

Complete contact information is available at: https://pubs.acs.org/10.1021/acsphyschemau.2c00012

Notes

The authors declare no competing financial interest.

■ ACKNOWLEDGMENTS

The authors thank Prof. K. Ohno (Tohoku University) and Prof. S. Maeda (Hokkaido University) for allowing us to use the GRRM program. K.F. wishes to dedicate this paper to late Prof. Mineo Kimura and late Prof. Yasutake Teraoka of Kyushu University. K.O. was supported by the Institute for Quantum Chemical Exploration (IQCE) Research Fellowships for Young Scientists. T.T. (Tsutsumi) was supported by Hokkaido University through the Program for Leading Graduate Schools (Hokkaido University "Ambitious Leader's Program") and grant-in-aid for Japan Society for the Promotion of Science (JSPS, Japan) Fellows grant number JP18J20856. This work was supported by JST CREST grant number JPMJCR1902, the Photo-excitonix Project in Hokkaido University, and the MEXT Doctoral program for the Data-Related InnoVation Expert Hokkaido University (D-DRIVE-HU) program. A part of calculations was performed at the Research Center for Computational Science, Okazaki, Japan. The GIBMS work was supported by the National Science Foundation grant CHE-1954142 (PBA).

■ ABBREVIATIONS

PES	potential energy surface
GRRM	global reaction route mapping

https://doi.org/10.1021/acsphyschemau.2c00012
ACS Phys. Chem Au XXXX, XXX, XXX−XXX

ADDF	anharmonic downward distortion following
TS	transition state
GIBMS	guided ion beam mass spectrometry
MD	molecular dynamics
SVP	sudden vector projection
RC	reaction coordinate.

REFERENCES

(1) Fukui, K. Formulation of the reaction coordinate. *J. Phys. Chem.* **1970**, *74*, 4161−4163.

(2) Maeda, S.; Harabuchi, Y.; Ono, Y.; Taketsugu, T.; Morokuma, K. Intrinsic reaction coordinate: Calculation, bifurcation, and automated search. *Int. J. Quantum Chem.* **2015**, *115*, 258−269.

(3) Ohno, K.; Maeda, S. A scaled hypersphere search method for the topography of reaction pathways on the potential energy surface. *Chem. Phys. Lett.* **2004**, *384*, 277−282.

(4) Maeda, S.; Taketsugu, T.; Morokuma, K.; Ohno, K. Anharmonic Downward Distortion Following for Automated Exploration of Quantum Chemical Potential Energy Surfaces. *Bull. Chem. Soc. Jpn.* **2014**, *87*, 1315−1334.

(5) Maeda, S.; Harabuchi, Y.; Takagi, M.; Taketsugu, T.; Morokuma, K. Artificial Force Induced Reaction (AFIR) Method for Exploring Quantum Chemical Potential Energy Surfaces. *Chem. Rec.* **2016**, *16*, 2232−2248.

(6) Maeda, S.; Ohno, K.; Morokuma, K. Systematic exploration of the mechanism of chemical reactions: the global reaction route mapping (GRRM) strategy using the ADDF and AFIR methods. *Phys. Chem. Chem. Phys.* **2013**, *15*, 3683−3701.

(7) Sumiya, Y.; Nagahata, Y.; Komatsuzaki, T.; Taketsugu, T.; Maeda, S. Kinetic Analysis for the Multistep Profiles of Organic Reactions: Significance of the Conformational Entropy on the Rate Constants of the Claisen Rearrangement. *J. Phys. Chem. A* **2015**, *119*, 11641−11649.

(8) Miller, W. H.; Handy, N. C.; Adams, J. E. Reaction path Hamiltonian for polyatomic molecules. *J. Chem. Phys.* **1980**, *72*, 99−112.

(9) Kato, S.; Morokuma, K. Potential energy characteristics and energy partitioning in chemical reactions: Ab initio MO study of four-centered elimination reaction $CH_3CH_2F \rightarrow CH_2{=}CH_2{+}HF$. *J. Chem. Phys.* **1980**, *73*, 3900−3914.

(10) Sun, L.; Song, K.; Hase, W. L. A S_N2 Reaction That Avoids Its Deep Potential Energy Minimum. *Science* **2002**, *296*, 875−878.

(11) López, J. G.; Vayner, G.; Lourderaj, U.; Addepalli, S. V.; Kato, S.; DeJong, W. A.; Windus, T. L.; Hase, W. L. A Direct Dynamics Trajectory Study of F^- + CH_3OOH Reactive Collisions Reveals a Major Non-IRC Reaction Path. *J. Am. Chem. Soc.* **2007**, *129*, 9976−9985.

(12) Blanksby, S. J.; Ellison, G. B.; Bierbaum, V. M.; Kato, S. Direct Evidence for Base-Mediated Decomposition of Alkyl Hydroperoxides (ROOH) in the Gas Phase. *J. Am. Chem. Soc.* **2002**, *124*, 3196−3197.

(13) Pham, H. V.; Houk, K. N. Diels−Alder Reactions of Allene with Benzene and Butadiene: Concerted, Stepwise, and Ambimodal Transition States. *J. Org. Chem.* **2014**, *79*, 8968−8976.

(14) Hare, S. R.; Tantillo, D. J. Post-Transition State Bifurcations Gain Momentum − Current State of the Field. *Pure Appl. Chem.* **2017**, *89*, 679−698.

(15) Tsutsumi, T.; Harabuchi, Y.; Ono, Y.; Maeda, S.; Taketsugu, T. Analyses of Trajectory On-the-Fly Based on the Global Reaction Route Map. *Phys. Chem. Chem. Phys.* **2018**, *20*, 1364−1372.

(16) Ervin, K. M.; Armentrout, P. B. Translational energy dependence of $Ar^+ + XY \rightarrow ArX^+ + Y$ (XY=H_2,D_2,HD) from thermal to 30 eV c.m. *J. Chem. Phys.* **1985**, *83*, 166−189.

(17) Armentrout, P. B. Kinetic energy dependence of ion-molecule reactions: guided ion beams and threshold measurements. *Int. J. Mass Spectrom.* **2000**, *200*, 219−241.

(18) Schultz, R. H.; Armentrout, P. B. Reactions of N^+_4 with rare gases from thermal to 10eV center-of-mass energy: collision-induced dissociation, charge transfer and ligand exchange. *Int. J. Mass Spectrom. Ion Process.* **1991**, *107*, 29−48.

(19) Schultz, R. H.; Crellin, K. C.; Armentrout, P. B. Sequential bond energies of iron carbonyl $Fe(CO)_x^+$ (x = 1-5): systematic effects on collision-induced dissociation measurements. *J. Am. Chem. Soc.* **1991**, *113*, 8590−8601.

(20) Teloy, E.; Gerlich, D. Integral cross sections for ion-molecule reactions. I. The guided beam technique. *Chem. Phys.* **1974**, *4*, 417−427.

(21) Daly, N. R. Scintillation Type Mass Spectrometer Ion Detector. *Rev. Sci. Instrum.* **1960**, *31*, 264−267.

(22) Chantry, P. J. Doppler Broadening in Beam Experiments. *J. Chem. Phys.* **1971**, *55*, 2746−2759.

(23) Lifshitz, C.; Wu, R. L. C.; Tiernan, T. O.; Terwilliger, D. T. Negative ion−molecule reactions of ozone and their implications on the thermochemistry of O_3^-. *J. Chem. Phys.* **1978**, *68*, 247−260.

(24) Chesnavich, W. J.; Bowers, M. T. Theory of translationally driven reactions. *J. Phys. Chem.* **1979**, *83*, 900−905.

(25) Muntean, F.; Armentrout, P. B. Guided ion beam study of collision-induced dissociation dynamics: integral and differential cross sections. *J. Chem. Phys.* **2001**, *115*, 1213.

(26) Armentrout, P. B. Not just a structural tool: the use of guided ion beam tandem mass spectrometry to determine thermochemistry. *J. Am. Soc. Mass Spectrom.* **2002**, *13*, 419−434.

(27) Armentrout, P. B. Reaction Threshold Energy Measurements. In *The Encyclopedia of Mass Spectrometry. Volume 1: Theory and Ion Chemistry*, Armentrout, P. B., Ed.; Elsevier: Amsterdam, 2003; pp 417−426.

(28) Armentrout, P. B. The Power of Accurate Energetics (or Thermochemistry: What is it Good for?). *J. Am. Soc. Mass Spectrom.* **2013**, *24*, 173.

(29) Dyke, J. M.; Lewis, A. E.; Morris, A. A photoelectron spectroscopic study of the ground state of CF^+ via the ionization process $CF^+(X^1\Sigma^+) \leftarrow CF(X^2\Pi)$. *J. Chem. Phys.* **1984**, *80*, 1382−1386.

(30) Ruscic, B.; Bross, D. H. Active Thermochemical Tables (ATcT) Values Based on Ver. 1.122g of the Thermochemical Network. available at ATcT.anl.gov (accessed June 10, 2021).

(31) Armentrout, P. B.; Simons, J. Understanding Heterolytic Bond Cleavage. *J. Am. Chem. Soc.* **1992**, *114*, 8627.

(32) Seeger, R.; Pople, J. A. Self-consistent molecular orbital methods. XVIII. Constraints and stability in Hartree−Fock theory. *J. Chem. Phys.* **1977**, *66*, 3045−3050.

(33) Bauernschmitt, R.; Ahlrichs, R. Stability analysis for solutions of the closed shell Kohn-Sham equation. *J. Chem. Phys.* **1996**, *104*, 9047−9052.

(34) Frisch, M. J., Trucks, G. W., Schlegel, H. B., Scuseria, G. E., Robb, M. A., Cheeseman, J. R., Scalmani, G., Barone, V., Mennucci, B., Petersson, G. A., Nakatsuji, H., Caricato, M., Li, X., Hratchian, H. P., Izmaylov, A. F., Bloino, J., Zheng, G., Sonnenberg, J. L., Hada, M., Ehara, M., Toyota, K., Fukuda, R., Hasegawa, J., Ishida, M., Nakajima, T., Honda, Y., Kitao, O., Nakai, H., Vreven, T., Montgomery, J. A., Jr., Peralta, J. E., Ogliaro, F., Bearpark, M., Heyd, J. J., Brothers, E., Kudin, K. N., Staroverov, V. N., Keith, T., Kobayashi, R., Normand, J., Raghavachari, K., Rendell, A., Burant, J. C., Iyengar, S. S., Tomasi, J., Cossi, M., Rega, N., Millam, J. M., Klene, M., Knox, J. E., Cross, J. B., Bakken, V., Adamo, C., Jaramillo, J., Gomperts, R., Stratmann, R. E., Yazyev, O., Austin, A. J., Cammi, R., Pomelli, C., Ochterski, J. W., Martin, R. L., Morokuma, K., Zakrzewski, V. G., Voth, G. A., Salvador, P., Dannenberg, J. J., Dapprich, S., Daniels, A. D., Farkas, O., Foresman, J. B., Ortiz, J. V., Cioslowski, J., Fox, D. J. *Gaussian 09*, Revision D.01; Gaussian, Inc.: Wallingford CT, 2013.

(35) Maeda, S., Harabuchi, Y., Osada, Y., Taketsugu, T., Morokuma, K.; Ohno, K. *GRRM14*, version 14.01, see https://iqce.jp/GRRM/index_e.shtml (accessed April 1, 2022).

(36) Nakai, H.; Yamauchi, Y.; Matsuda, A.; Okada, Y.; Takeuchi, K. Ab initio MD simulation of collision reaction between ammonia cluster ion and ammonia monomer. *J. Mol. Struct.* **2002**, *592*, 61−67.

(37) Martínez-Núñez, E.; Fernández-Ramos, A.; Vázquez, S. A.; Marques, J. M. C.; Xue, M.; Hase, W. L. Quasiclassical dynamics simulation of the collision-induced dissociation of $Cr(CO)_6^+$ with Xe. *J. Chem. Phys.* **2005**, *123*, 154311.

https://doi.org/10.1021/acsphyschemau.2c00012
ACS Phys. Chem Au XXXX, XXX, XXX−XXX

(38) Wang, Y.; Hase, W. L.; Wang, H. Trajectory studies of S_N2 nucleophilic substitution. IX. Microscopic reaction pathways and kinetics for $Cl^- + CH_3Br$. *J. Chem. Phys.* **2003**, *118*, 2688−2695.
(39) Zhang, J.; Lourderaj, U.; Sun, R.; Mikosch, J.; Wester, R.; Hase, W. L. Simulation studies of the $Cl^- + CH_3I$ S_N2 nucleophilic substitution reaction: Comparison with ion imaging experiments. *J. Chem. Phys.* **2013**, *138*, 114309.
(40) Wester, R. Velocity map imaging of ion-molecule reactions. *Phys. Chem. Chem. Phys.* **2014**, *16*, 396−405.
(41) Wester, R. Fifty years of nucleophilic substitution in the gas phase. *Mass Spectrom. Rev.* **2021**, 1−18.
(42) Jiang, B.; Guo, H. Relative efficacy of vibrational vs. translational excitation in promoting atom-diatom reactivity: Rigorous examination of Polanyi's rules and proposition of sudden vector projection (SVP) model. *J. Chem. Phys.* **2013**, *138*, 234104.
(43) Polanyi, J. C. Some Concepts in Reaction Dynamics. *Acc. Chem. Res.* **1972**, *5*, 161−168.
(44) Guo, H.; Jiang, B. The Sudden Vector Projection Model for Reactivity: Mode Specificity and Bond Selectivity Made Simple. *Acc. Chem. Res.* **2014**, *47*, 3679−3685.
(45) Li, J.; Guo, H. Mode Specificity and Product Energy Disposal in Unimolecular Reactions: Insights from the Sudden Vector Projection Model. *J. Phys. Chem. A* **2014**, *118*, 2419−2425.
(46) Stei, M.; Carrascosa, E.; Dörfler, A.; Meyer, J.; Olasz, B.; Czakó, G.; Li, A.; Guo, H.; Wester, R. Stretching vibration is a spectator in nucleophilic substitution. *Sci. Adv.* **2018**, *4*, No. eaas9544.
(47) Kabsch, W. A solution for the best rotation to relate two sets of vectors. *Acta Cryst. A* **1976**, *32*, 922−923.
(48) Harabuchi, Y., Okai, M., Yamamoto, R., Tsutsumi, T., Ono, Y., Taketsugu, T. *SPPR, a Developmental Version*; Hokkaido University: Sapporo, Japan, 2020.
(49) Verlet, L. Computer ″Experiments″ on Classical Fluids. I. Thermodynamical Properties of Lennard-Jones Molecules. *Phys. Rev.* **1967**, *159*, 98.
(50) Carpenter, B. K. Dynamic Matching: The Cause of Inversion of Configuration in the [1,3] Sigmatropic Migration? *J. Am. Chem. Soc.* **1995**, *117*, 6336−6344.
(51) Wang, Z.; Hirschi, J. S.; Singleton, D. A. Recrossing and Dynamic Matching Effects on Selectivity in a Diels-Alder Reaction. *Angew. Chem., Int. Ed.* **2009**, *48*, 9156−9159.
(52) de Sainte Claire, P.; Hase, W. L. Thresholds for the Collision-Induced Dissociation of Clusters by Rare Gas Impact. *J. Phys. Chem.* **1996**, *100*, 8190−8196.
(53) DeTuri, V. F.; Hintz, P. A.; Ervin, K. M. Translational Activation of the S_N2 Nucleophilic Displacement Reactions $Cl^- + CH_3Cl$ (CD_3Cl) → $ClCH_3$ ($ClCD_3$) + Cl^-: A Guided Ion Beam Study. *J. Phys. Chem. A* **1997**, *101*, 5969−5986.
(54) Karmakar, S.; Keshavamurthy, S. Intramolecular vibrational energy redistribution and the quantum ergodicity transition: a phase space perspective. *Phys. Chem. Chem. Phys.* **2020**, *22*, 11139−11173.

https://doi.org/10.1021/acsphyschemau.2c00012
ACS Phys. Chem Au XXXX, XXX, XXX−XXX